Angular correlations in deep exclusive photo-production of lepton pairs and tools for data analysis

Marie Boër,*
Catholic University of America, Washington, D.C. 20064.

March 20, 2018

Abstract

Deep exclusive photo-production of lepton pairs off the nucleon, the $\gamma N \to \gamma^* N \to e^+e^- N$ reaction, is sensitive to the nucleon partonic structure at high γ^* virtuallity. This reaction is dominated by the Bethe-Heitler like process where the incoming real photon splits into a lepton pair in the nucleon field. It interfers with Timelike Compton Scattering, where a real photon is scattered off a quark from the nucleon and a virtual photon is emitted, then decays into a lepton pair. We studied the correlations between decay angles of the leptons, and between decay angles and kinematic variables in the lab frame. The goal of this work is to make predictions for designing future experiments, and to accompany current data analysis involving exclusive lepton pairs production. We present our interpretations of the lepton pair angular behaviour, we discuss the kinematic and angular dependencies of the unpolarized BH cross section, and the correlations between different variables. We propose tools for data analysis. All calculations have been made at typical kinematic for JLab 12 GeV experiments and our results can be applied for any experiment in an equivalent kinematic domain.

1 Introduction

The deeply exclusive photoproduction of a lepton pair ($\gamma N \to e^+e^- N$, where e is any lepton and N is a nucleon), involves two processes:

- The Bethe-Heitler like process (BH) corresponds to the splitting of a real photon in the nucleon field (Fig. 1). It is parameterized by nucleon Form Factors (FFs).
- The Compton-like process (TCS for Timelike Compton Scattering) corresponds to the scattering of a real photon off a quark, where a high virtuality photon is emitted. The final photon decays into a lepton pair (Fig. 2). This process is parameterized by Generalized Parton Distributions of the nucleon (GPDs).

This note is intended to accompany experimental studies of dilepton pair exclusive production at Jefferson Laboratory's 12 GeV experiments, such as TCS+BH studies and exclusive meson production where the meson is decaying into a lepton pair. We did our calculations in the mass range

*contact: mboer@jlab.org

for the pair from 2 to 3 GeV, corresponding to an accessible kinematic for these experiments, and allowing to stay away from resonances in the dilepton mass spectra (J/Ψ, ρ'...). Our considerations on angular correlations in this work are based only on Bethe-Heitler behavior, which is largely dominant compared to TCS at such kinematics [1]. Therefore, we will neglect in the rest of this note interferences with BH process, including TCS. We assume that interferences are small and not strongly affecting the angular behavior of the leptons, mostly coming from BH for an unpolarized beam and target.

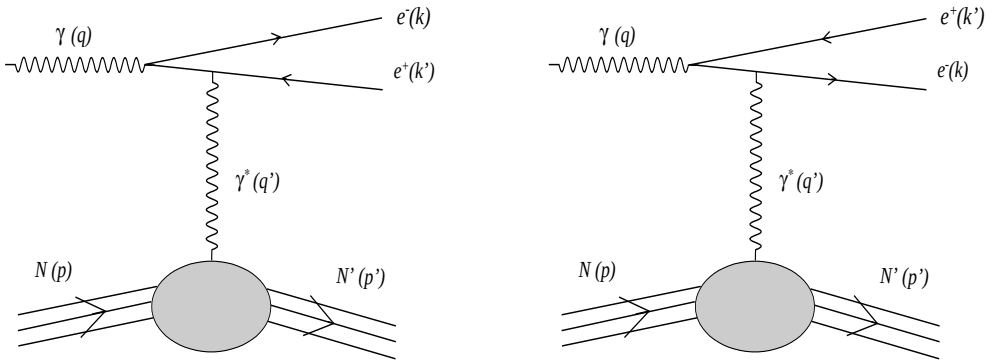

Figure 1: Bethe-Heitler leading order and leading twist diagrams.

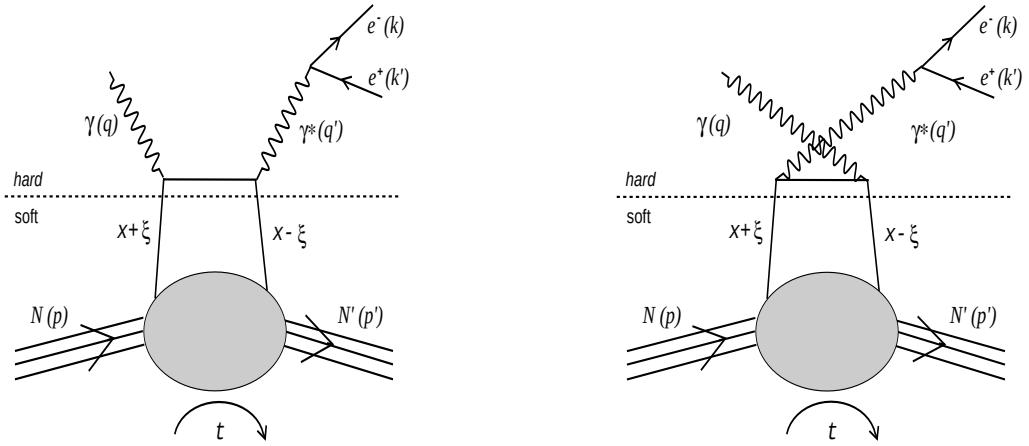

Figure 2: TCS leading order and leading twist handbag diagrams.

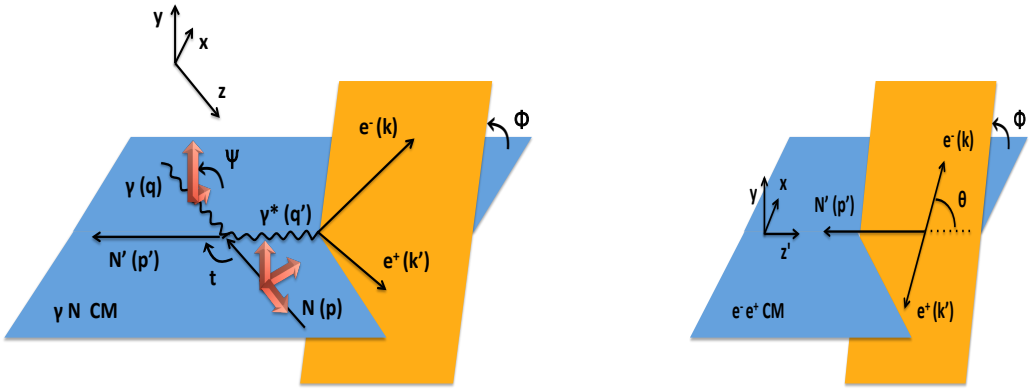

Figure 3: Scheme of the TCS reaction in the nucleon-photon center of mass frame (left panel) and in the final photon rest frame (right panel). The momentum of incoming and outgoing nucleon, real and virtual photon, electron and positron are indicated by letters p, p', q, q', k and k', respectively. Left panel: we indicated the angle ϕ_{CM} between the lepton decay plane and the reaction plane. We also indicated by red arrows the possible orientations of beam and target spin. Right panel: ϕ_{CM} angle is conserved in the boost from γN to γ^* CM frames. θ_{CM} is the angle between the lepton direction and the boost axis, defined by γ^* direction in γN CM frame.

2 Formalism

2.1 Unpolarized BH cross section

The formalism used in this study is detailed in [1]. Unpolarized cross section for exclusive dilepton photoproduction depends on five independent variables. At fixed beam energy, averaging over beam, initial and final nucleon helicities, we can express the 4-differential BH+TCS unpolarized cross section as

$$\frac{d^4\sigma}{dQ'^2 dt d\Omega}(\gamma p \to p' e^+ e^-) = \frac{1}{2\pi^4}\frac{1}{64}\frac{1}{(2m_N E_\gamma)^2} \mid T^{BH} + T^{TCS} \mid^2,$$

where the $\mid T^{BH} + T^{TCS} \mid^2$ term corresponds to BH and TCS amplitudes. We expressed the cross section as a function of the momentum transfer to the nucleon t, the final photon virtuality Q'^2, the nucleon mass m_N, the incoming photon energy E_γ and the decay angle of the final electron in the virtual photon CM frame $d\Omega = d\phi_{CM} dcos(\theta_{CM})$. These angles are represented on Fig. 3. Left panel is a scheme of the reaction in the CM frame of the incoming photon and the proton. Variables and angles represented in the scheme are explicit in the legend. Fig. 3 (right panel) shows the angles in the virtual photon CM frame. The longitudinal axis for boosting between the two frames is the reference for the final electron polar angle.

As mentionned above, we are neglecting in this work the TCS and its interference with BH. Following the formalism from [1], BH amplitude can be expressed as

$$T^{BH} = -\frac{e^3}{\Delta^2}\,\bar{N}\,\Gamma^\nu\,N\,\epsilon^\mu(q)\,\bar{u}(k)\,\left(\gamma_\mu\frac{\not{k}-\not{q}}{(k-q)^2}\gamma_\nu+\gamma_\nu\frac{\not{q}-\not{k}'}{(q-k')^2}\gamma_\mu\right)\,v(k'), \tag{1}$$

where the 4-vectors q, k, k' respectively correspond to the photon, the electron and the positron. N corresponds to the nucleon spinor and Δ is the proton momentum transfer. The virtual photon-proton electromagnetic vertex matrix can be expressed as a function of Dirac (F_1) and Pauli (F_2) form factors

$$\Gamma^\nu = \gamma^\nu\,F_1(t) + \frac{i\sigma^{\nu\rho}\Delta_\rho}{2\,m_N}\,F_2(t), \tag{2}$$

which are related to the electric (G_E) and magnetic (G_M) form factors as

$$F_1 = \frac{G_E+\tau G_M}{1+\tau},\;\; F_2 = \frac{G_M-G_E}{1+\tau}, \tag{3}$$

where

$$\tau = \frac{Q'^2}{4m_N^2}. \tag{4}$$

2.2 Parametrization and systematic uncertainties on BH calculations

We performed our calculations using the electric form factor parametrization from [2] and magnetic form factor parametrization from [3]. We showed that differences in the calculated unpolarized BH cross section from various form factor parametrizations are up to 5% [1]. A comparison of form factors from different parametrizations is displayed on Fig. 4.

3 Kinematic and angular dependencies of the unpolarized BH cross section

3.1 Correlation between kinematic variables

We display on Fig. 5 the $-t$ and Q'^2 dependence of the unpolarized BH cross section. Calculations have been done at typical JLab 12 GeV experimental energies. Fig. 6 shows the correlations between t, Q'^{2} and ξ. The longitudinal momentum transfer ξ can be expressed as a function of the center of mass squared momentum s and Q'^2, as $\xi = \frac{Q'^2}{2s-Q'^2}$. Events displayed in these distributions have been generated with [7], using the same calculations as for previous figures of this note. The kinematic domain for generating events has been restricted to:

- 8.5 < E_γ<10.5 GeV,
- 4 < Q'^{2} < 9 GeV^2,
- .04 < -t < 0.8 GeV^2.

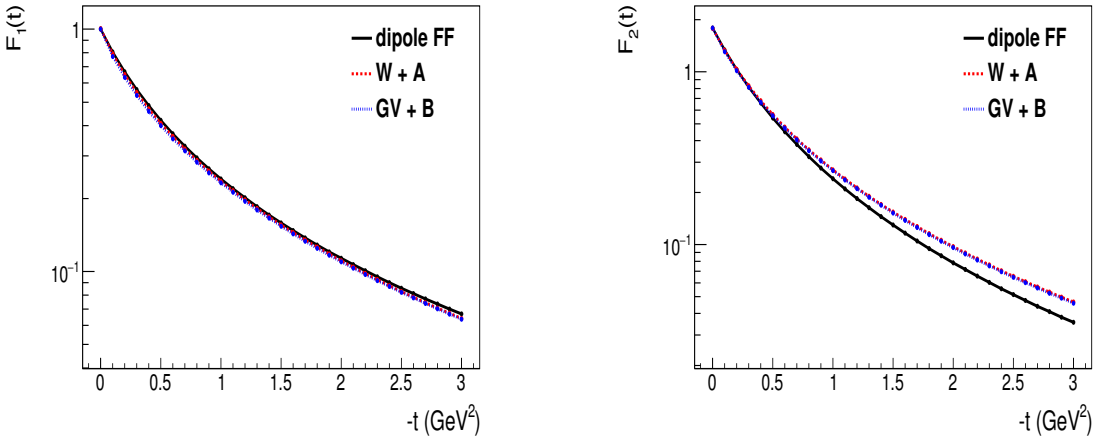

Figure 4: Comparison for Dirac (left panel) and Pauli (right panel) form factors from 3 different combinations of electric and magnetic form factor parametrizations. The 3 curves correspond, according to the notations of the legend to parametrizations from: 1) "dipole FF" = dipole form factor parametrization [4], 2) "W + A" = respectively [5] and [6] for G_E and G_M, 3) "GV + B" = respectively [2] and [3] for G_E and G_M.

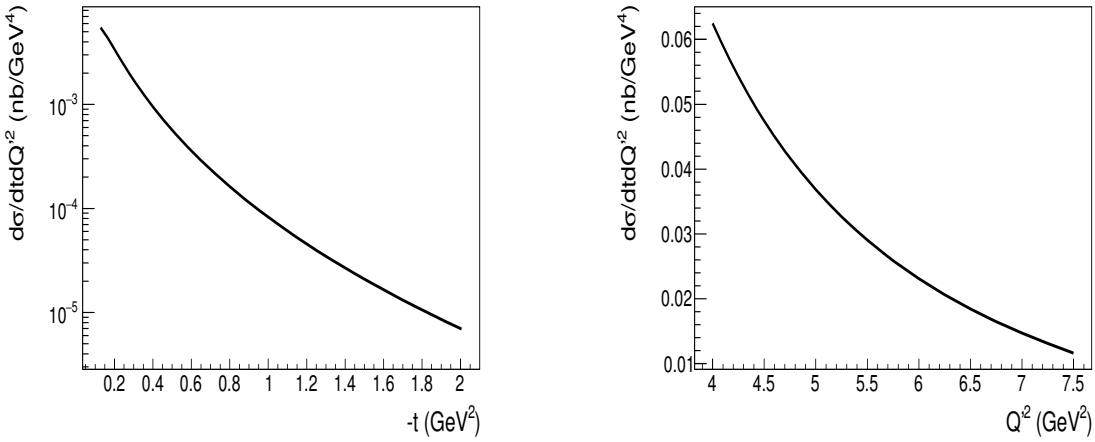

Figure 5: BH cross section as a function of t (left panel) and Q'^2 = 5 GeV^2 (right panel) at E$_\gamma$=9.5 GeV, for $0 < \phi_{CM} < 360°$ and $45° < \theta_{CM} < 135°$. Respectively, -t=0.3 GeV^2 and Q'^{2}=5 GeV^2.

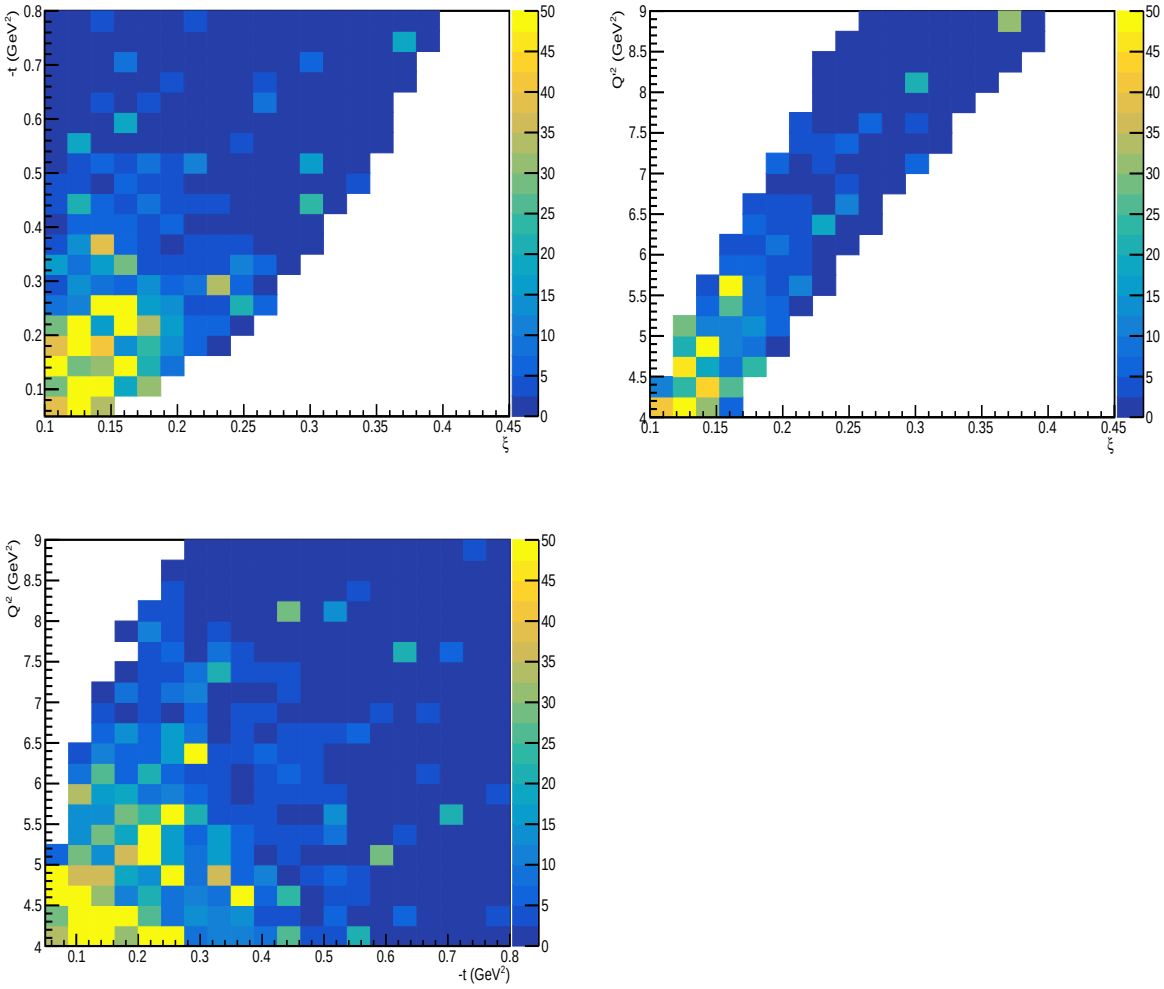

Figure 6: Top left: -t as a function of ξ, top right: Q'^2 as a function of ξ, bottom left: Q'^2 as a function of -t. The beam energy has been limited to 8.5 < E_γ<10.5 GeV. The weights are proportionnal to the unpolarized cross section.

3.2 Peaks in BH angular distributions and interpretations

Angular dependence of the lepton pair production can be understood with the BH propagators of eq.1. In the lab frame or in the γN CM frame, if one of the leptons are emitted along the beam direction, one of the terms becomes very large. It is then proportional to $\approx \frac{1}{m_e}$ (m_e is the lepton mass). At these limits, one of the two BH diagrams is largely dominant compared to the other one. One of the leptons takes most of the energy of the virtual photon and is emitted at very low angle ($\sim 0^\circ$), while the other one is emitted at large angle ($\sim 180^\circ$) with a very low momentum. The cross section drastically increases next to these limits and sharp peaks are observed in angular distributions, which will be discussed later in this note. Azimuthal distributions (ϕ_{CM}) are also strongly affected by this effect: one lepton going to the beam direction is forcing all particles to be emitted in the same plane (see Fig. 3).

We expressed the cross sections as a function of the virtual photon CM frame electron angles ϕ_{CM} and θ_{CM} (eq. 1). The angle ϕ_{CM} is conserved in the boost from γN CM frame, θ_{CM} (boost axis, electron polar angle) is correlated to θ_{lab} for a given $\Theta_{\gamma\gamma^*}$ angle (angle between incoming and outgoing photon). At small $\Theta_{\gamma\gamma^*}$ (t_{min} limit), we have the following effect:

- $\theta_{CM} \to 0$, i.e. e^- is emitted along the beam direction, the diagram on right panel on Fig. 1 largely dominates. A sharp peak will be observed in the cross section at $\theta_{CM} \to 0^\circ$ and $\phi_{CM} = 180^\circ$.
- $\theta_{CM} \to 180^\circ$, i.e. e^+ is emitted along the beam direction, the diagram on left panel on Fig. 1 largely dominates. A sharp peak will be observed in the cross section at $\theta_{CM} \to 180^\circ$ and $\phi_{CM} = 0^\circ$.

At $\Theta_{\gamma\gamma^*}$ larger than zero, the position of the peaks in θ_{CM} distribution depends on the kinematics (E_γ, t, Q'^2). The correlation between $\Theta_{\gamma\gamma^*}$ and t at fixed E_γ and Q'^2 is presented on Fig. 7 (left panel). The cross section dependence in $\Theta_{\gamma\gamma^*}$ (Fig. 7, right panel) reflects the t dependence of Fig. 5.

3.3 Distributions in ϕ_{CM} and correlation with θ_{CM}

At fixed θ_{CM} and fixed kinematic, the ϕ_{CM} distributions displayed in Fig. 8 are illustrating the discussion of section 3.2. At $\theta_{CM} = 10^\circ$ and $\theta_{CM} = 170^\circ$, cross sections are very large, and peaks respectivelly at $\phi_{CM} = 90^\circ$ and $\phi_{CM} = 0^\circ$ are observed. At $\theta_{CM} = 90^\circ$, the two BH diagrams have the same contribution and two peaks are observed at $\phi_{CM} = 0^\circ$ and $\phi_{CM} = 90^\circ$. In addition, the cross section is significantly smaller at $\theta_{CM} = 90^\circ$ when approching the limits $\theta_{CM} \to 0$ and $\theta_{CM} \to 90^\circ$. We refer to [8] (Fig. 6) for calculations at various ϕ_{CM} and θ_{CM} angles and related discussion.

The same effect is illustrated in Fig. 9, presenting distributions in ϕ_{CM}, where θ_{CM} has been integrated in asymmetric ranges over θ_{CM} (one diagram dominates). At these kinematics, the BH peaks are at $\theta_{CM} \sim 20^\circ$ and $\theta_{CM} \sim 160^\circ$, explaining that the curve corresponding to $20^\circ < \phi_{CM} < 30^\circ$ presents the largest cross section. In the perspective of experimental measurements, integrating calculations over a symmetric range around $\theta_{CM} = 90^\circ$, away from BH peaks, presents the advantage of having the same contribution from the two diagrams in the integrated cross section while enhancing the statistic in each bin for displaying distributions in other variables in the data.

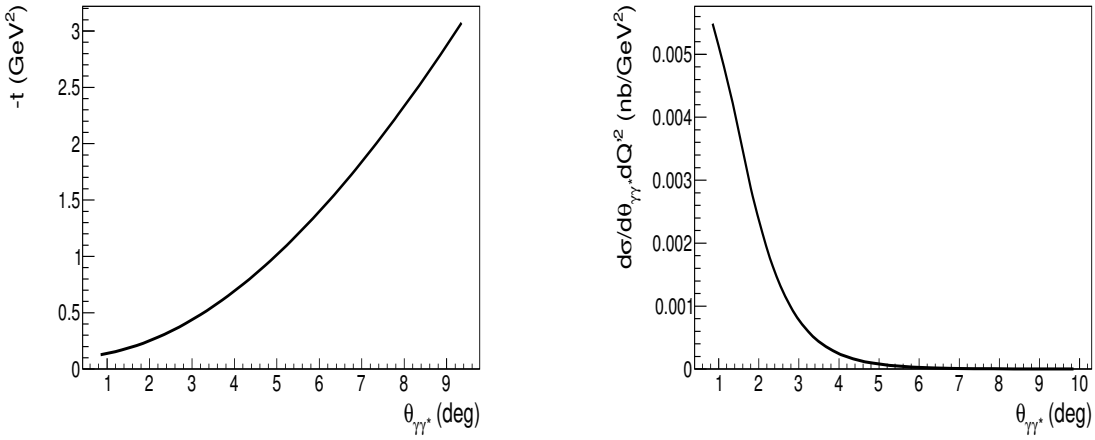

Figure 7: BH cross section as a function of t (left panel) and Q'^2 = 5 GeV^2 (right panel) at E$_\gamma$=9.5 GeV, for $0 < \phi_{CM} < 360°$ and $45° < \theta_{CM} < 135°$. Respectively, -t=0.3 GeV^2 and Q$'^2$=5 GeV^2.

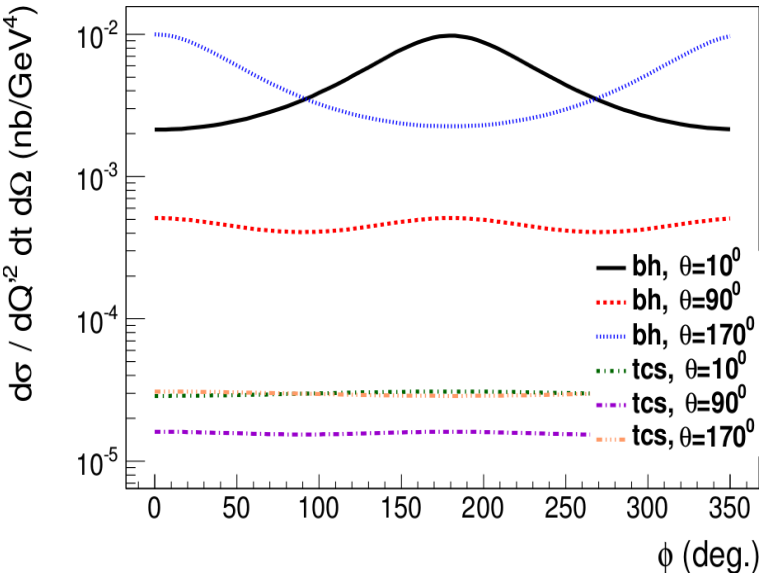

Figure 8: BH cross section as a function of ϕ at Q'^2 = 7 GeV^2, -t=0.4 GeV^2, ξ=0.2, for $\theta_{CM} = 10°$, $\theta_{CM} = 170°$ and $\theta_{CM} = 90°$. TCS curves have been included as well but are not commented in the text.

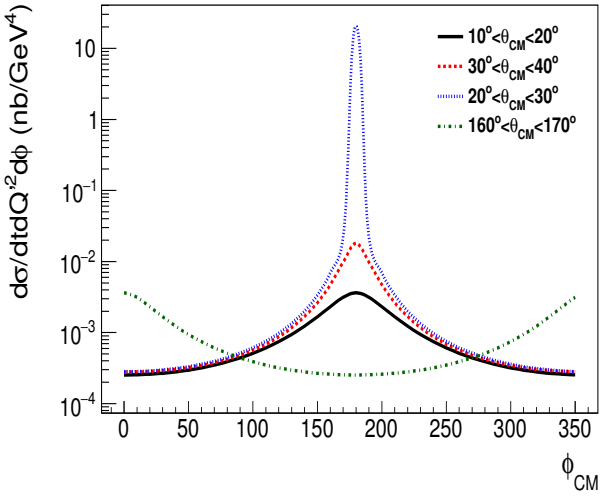

Figure 9: BH cross section as a function of ϕ at Q'^2 = 5 GeV^2, -t=0.3 GeV^2, E$_\gamma$=9.5 GeV, and integrated over θ_{CM} on various ranges (colored curves).

3.4 Distributions in θ_{CM} and correlation with kinematic variables

As discussed in section 3.2, the θ_{CM} distribution and position of BH peaks is correlated to the angle $\Theta_{\gamma\gamma^*}$, which depends on t, Q'^2 and E_γ. For kinematics with $-t \to t_{min}$, the peaks are observed at $\theta_{CM} \to 0$ and $\theta_{CM} \to 180°$. For larger $-t$, and for different values of Q'^2 and E_γ, the peaks are observed at different values, approching $90°$ for the large -t limit. We display on Fig. 10 distributions in θ_{CM} where ϕ_{CM} has been integrated from 0 to 360°. The curves correspond to different values of t. We shall mention that the value of cross sections inside the peaks (next to the limits) are not calculated with an infinite precision, and thus we observe a different size of the two peaks, while they are supposed to be equal. The rest of the distribution is symmetric as expected. It is a consequence of the sharp increase of the BH cross section next to the peaks, which can be solved by increasing the precision of the integral over ϕ_{CM} at the cost of a large number of steps and computation time. We will discuss this technical statement in section 4.1. Beyond this observation, as expected, we see that the BH peaks are at $\theta_{CM} \to 0$ and $\theta_{CM} \to 180°$ when approching t_{min}, and at values between these two extrems limits for larger values of $-t$. We also observe that the sharp increase of the cross section next to the peaks is limited for larger value of $-t$. At t_{min}, the cross section can increase by several orders of magnitude within a few degrees in θ_{CM} or ϕ_{CM} range.

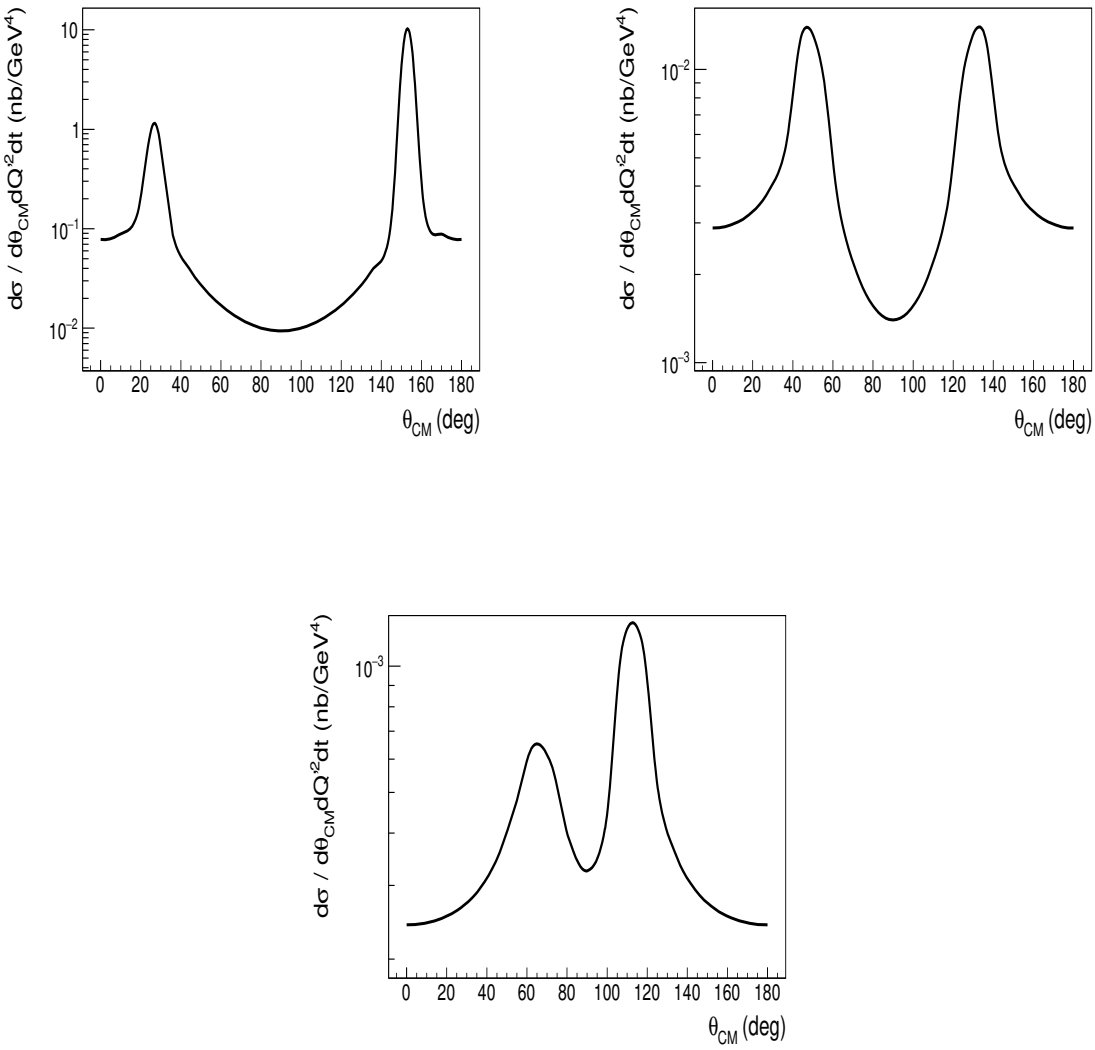

Figure 10: BH cross section as a function of θ_{CM} for E_γ=9.5 GeV, Q'^2 = 5 GeV^2, $0 < \phi_{CM} < 360^\circ$ and -t=0.3 GeV^2 (top left panel), -t=0.8 GeV^2 (top right panel), -t=1.5 GeV^2 (bottom panel).

4 Tools for data analysis

4.1 Limited statistic data sample

While BH cross sections can be calculated for any kinematic or angular fixed values, a discretized problem with limited bin width will be affected by the very fast increase of the cross section next to the peaks in the angular distributions. As we have seen in Fig. 10, where the integration over ϕ_{CM} has been performed with limited steps (gaus method), we don't reproduce exactly the same integrated cross section for the two peaks. It can be achieved by putting an enormous amount of steps in the integrals in ϕ_{CM}. Experimental and Monte-Carlo data are also integrating cross sections over the width of the bins they are displayed into. A sufficient amounts of simulations can be generated in order to achieve a reasonable precision for predicted cross sections from Monte-Carlo. However, experimental data are limited in statistics, and the exact kinematics of the events are known only up to the resolution precision. Experimental data are naturally "integrating" the cross section over a certain bin width, which cannot be thinner than the resolution in different variables. To fit these data, we need to integrate cross sections over the width of the bins they are presented into. As a consequence, it is not possible to achieve comparison with reasonable systematic uncertainties between experimental data having limited statistics and calculations when the cross sections are variating very fast over a single bin. Therefore, for fitting data with BH calculations, we have to stay away from BH peaks in the (θ_{CM}, ϕ_{CM}) distribution, where cross sections are typically increasing by more than two orders of magnitude within a single bin.

4.2 Angular cuts

To reproduce experimental conditions (limited statistics, broad kinematic range) and get the position of the BH peaks, we computed BH cross sections as a function of θ_{CM} at fixed values of E_γ, t and Q'^2. We integrated the cross sections over ϕ_{CM} with a limited number of steps. We perfomed calculations for two values of θ_{CM} symmetric around $\theta_{CM} = 90°$ with 5° steps in θ_{CM}: 85° and 95°, 80° and 100°... The results are expected to be the same for the two symmetric values of θ_{CM}. However, we observed (see Fig. 10) that calculations fail next to the peaks. We set as a condition to position the peaks and determine the region where we cannot fit data with reasonable errors, the observation of results being different by more than 5%. It defines the values of θ_{min} and θ_{max}, respectively the starts of the two steep slopes in θ_{CM} distribution. We reproduced the same exercise for different values of E_γ, t and Q'^2. Values of θ_{max} for $E_\gamma = 9.5$ GeV, as a function of $-t$ and Q'^2 are displayed on Fig. 11. Tables from which these projections are extracted from are available on the JLab ifarm machine:

- $/work/halla/solid/mboer/public/analysis\_tools/cut\_tables/scanBHsing\_fullrange.dat$ (0.02<-t<1.02 GeV^2)
- $/work/halla/solid/mboer/public/analysis\_tools/cut\_tables/scanBHsing\_t02\_fullrange.dat$ (0.02<-t<2.02 GeV^2)

The format of these tables is: E_γ (GeV), -t (GeV^2, Q'^2 (GeV^2), $\theta_{min}(degree)$. The upper limit is given by $\theta_{max} = 180° - \theta_{min}$.

We strongly recommend to cut the θ_{CM} range of any measurement of BH (+interfering processes) to $\theta_{min} < \theta_{CM} < \theta_{max}$ to avoid the peaks for measurements with cross sections integrated over ϕ_{CM} . For measurements binned in both ϕ_{CM} and θ_{CM}, we reproduced the same exercise by integrating cross sections over different ranges in ϕ_{CM} ($0 \pm 10°$, $0 \pm 20°$, $180° \pm 30°$...). We conclude that the peaks can be avoided by 2-dimensional cuts in ϕ_{CM} and θ_{CM} such as:

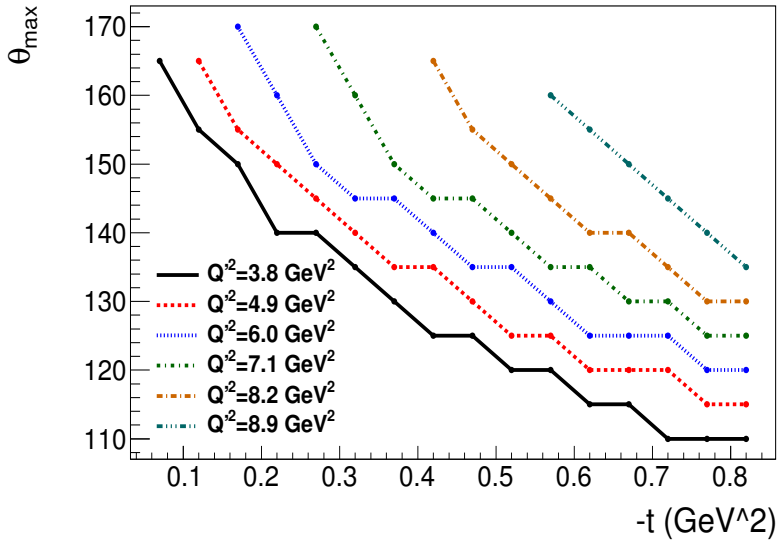

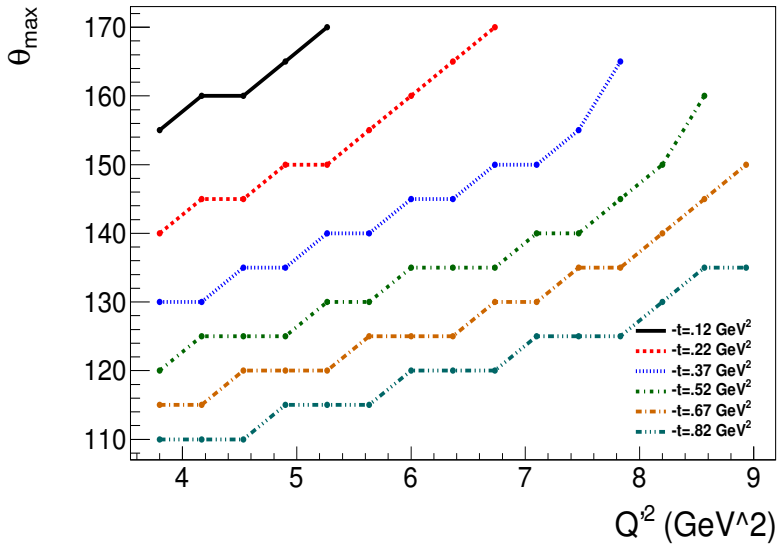

Figure 11: Values of θ_{max} for a fix beam energy $E_\gamma = 9.5$ GeV, as a function of t for different values of Q'^2 (top panel) and as a function of Q'^2 for different values of $-t$ (bottom panel).

- if (θ_{CM}<θ_{min} and $150^\circ < \phi_{CM} < 210^\circ$), the event has to be rejected,
- if (θ_{CM}>θ_{max} and $-30^\circ < \phi_{CM} < +30^\circ$, the event has to be rejected,
- otherwise the event can be kept and results can be fitted with reasonnable systematic errors.

The cut in ϕ_{CM} proposed here can be adjusted with the value of t: for $t \to t_{min}$, peaks are narrower and the cut can be limited to $\pm 20^\circ$ while it can be wider for larger $-t$ values.

5 Impact of cross sections and angular cuts in lab frame

5.1 Correlation between the electron and the positron angles and momentum in the lab frame

We display in Fig. 12 the asymmetries between angles (θ_{lab}, ϕ_{lab}) and momentum (P_{lab}) of the electron and the positron in the lab frame. These asymmetries are defined by

$$\frac{\Delta\theta_{lab}}{<\theta_{lab}>} = \frac{\theta_{lab}(e^-) - \theta_{lab}(e^+)}{\theta_{lab}(e^-) + \theta_{lab}(e^+)}, \tag{5}$$

and similarly for the other variables. The $\frac{\Delta\theta_{lab}}{<\theta_{lab}>}$ and $\frac{\Delta P_{lab}}{<P_{lab}>}$ distributions are reflecting the interpretations of section 3.2: if one lepton takes more energy, it is scattered at lower angle with larger momentum while the other one is scattered at large angle with lower momentum. Therefore, these distributions will present maximal asymmetries for larger cross sections. The $\frac{\Delta\phi_{lab}}{<\phi_{lab}>}$ distribution peaks at $\phi_{lab} = \pm 0.5$ are correlated to these asymmetric decays.

5.2 Correlation between θ_{CM} and θ_{lab}

We display on Fig. 13 the θ_{CM} versus θ_{lab} distribution of generated events for typical JLab 12 GeV kinematics (same sample as previous figures). Distributions are averaged over all kinematic variables but θ_{CM}. The weights are proportional to the cross section: the higher cross sections (color = yellow) observed in the lowest bin in θ_{lab} correspond to the BH peak for the electron scattered along the beam direction. The higher cross sections for larger θ_{lab} are a consequence of the correlation with the other BH peak: if the positron takes most of the available energy, the electron is scattered with lower momentum at larger lab angle ($\theta_{lab} \to 180^\circ$).

5.3 Acceptance and impact of the cuts

With actual spectrometer acceptance, most of events next to the BH peaks are naturally rejected: and low angle leptons are too close to the beam line to be detected, low momentum leptons don't have enough energy to pass calorimeter thresholds and/or be detected. Therefore, most current and future experiments will naturally avoid the peaks thanks to acceptance limitations, before applying the cuts proposed in section 4.2. We display on Fig. 14 the 2-dimensional distributions of generated data as a function of ϕ_{CM} and θ_{CM} before and after applying a $\theta_{lab} = 6^\circ$ angular threshold and a $E = 0.4$ GeV energy threshold on the two leptons. Event weights are proportionnal to the cross section. The regions of highest predicted cross sections (BH peaks, in yellow), are rejected by these naive acceptance cuts. The angular range that we defined for measurement after cuts in θ_{min} and θ_{max} is matching the acceptance of typical spectrometers. The statistical losses from the cuts will be limited by acceptance effects.

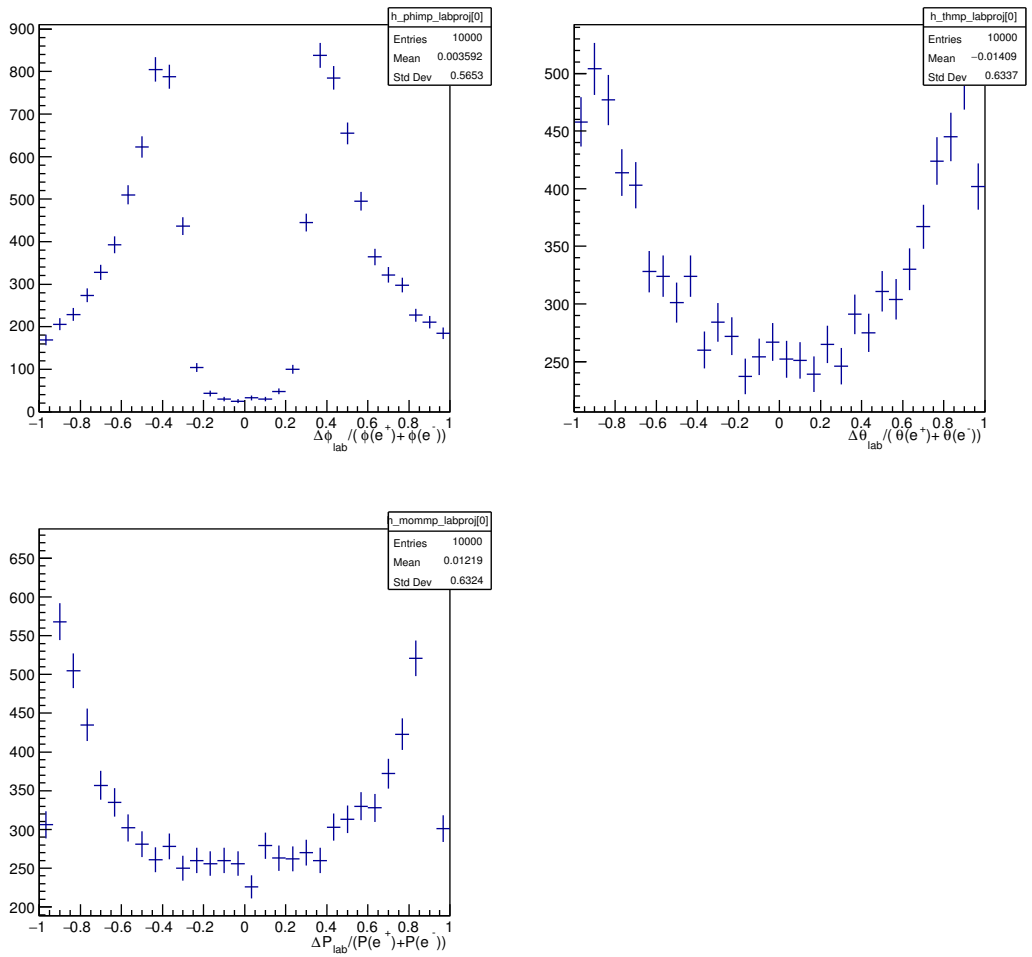

Figure 12: Asymmetries in lab frame between the scattered electron and positron. Top left: $\frac{\Delta\phi_{lab}}{<\phi_{lab}>}$, top right: $\frac{\Delta\theta_{lab}}{<\theta_{lab}>}$, bottom left: $\frac{\Delta P_{lab}}{<P_{lab}>}$.

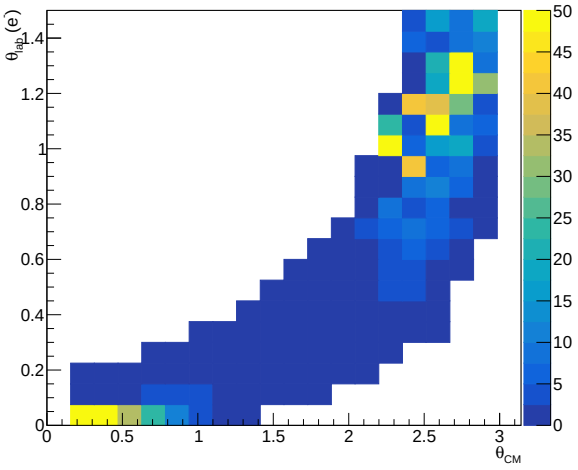

Figure 13: Distribution of θ_{CM} versus θ_{lab} for the scattered electron. Monte-Carlo data.

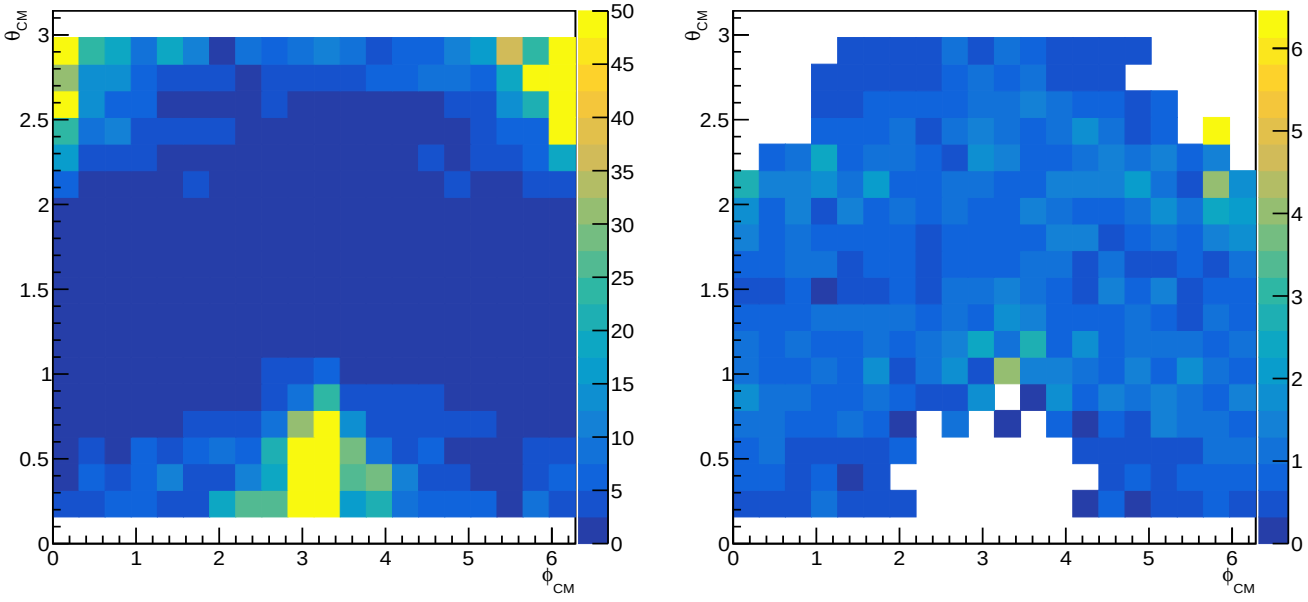

Figure 14: Distribution of generated events with weights proportionnal to the unpolarized cross section as a function of θ_{CM} and ϕ_{CM}. Left: all generated events, Right: angular threshold $theta_{lab} > 6^{\circ}$ and energy threshold $E > 0.4$ GeV.

6 Conclusion

We presented in this note our studies and interpretations of angular correlations in the Bethe-Heitler reaction. We proposed analysis tools to select angular regions where the comparision between experimental data and calculations can be achieved with reasonable statistical uncertainties. Our methods can be used for any exclusive dilepton pair production measurements involving Bethe-Heitler, such as Timelike Compton Scattering or exclusive meson production. We demonstrated that the impact of the proposed cuts is limited with typical spectrometer acceptance.

References

[1] M. Boër, M. Guidal and M. Vanderhaeghen, Eur. Phys. J. A **51** (2015) no.8, 103.

[2] P. A. M. Guichon and M. Vanderhaeghen, Phys. Rev. Lett. **91** (2003) 142303

[3] E. J. Brash, A. Kozlov, S. Li and G. M. Huber, Phys. Rev. C **65** (2002) 051001

[4] M. Guidal, Dipole form factors parametrization (private communication).

[5] O. Gayou *et al.* [Jefferson Lab Hall A Collaboration], Phys. Rev. Lett. **88** (2002) 092301

[6] J. Arrington, Phys. Rev. C **69** (2004) 022201

[7] M. Boër, DEEPGen: polarized BH+TCS event generator, `https://hallaweb.jlab.org/wiki/index.php/DDVCS_and_TCS_event_generator` (2015).

[8] M. Boër, M. Guidal and M. Vanderhaeghen, arXiv:1501.00270 [hep-ph].